nature astronomy

Article

https://doi.org/10.1038/s41550-023-01951-9

Azimuthal C/O variations in a planet-forming disk

Received: 31 October 2022

Accepted: 21 March 2023

Published online: 20 April 2023

Check for updates

Luke Keyte[1], Mihkel Kama[1,2], Alice S. Booth[3], Edwin A. Bergin[4], L. Ilsedore Cleeves[5], Ewine F. van Dishoeck[3,6], Maria N. Drozdovskaya[7], Kenji Furuya[8], Jonathan Rawlings[1], Oliver Shorttle[9] & Catherine Walsh[10]

The elemental carbon-to-oxygen ratio (C/O) in the atmosphere of a giant planet is a promising diagnostic of that planet's formation history in a protoplanetary disk. Alongside efforts in the exoplanet community to measure the C/O ratio in planetary atmospheres, observational and theoretical studies of disks are increasingly focused on understanding how the gas-phase C/O ratio varies both with radial location and between disks. This is mostly tied to the icelines of major volatile carriers such as CO and H_2O. Using ALMA observations of CS and SO, we have found evidence for an entirely unexpected type of C/O variation in the protoplanetary disk around HD 100546: an azimuthal variation from a typical, oxygen-dominated ratio (C/O ≈ 0.5) to a carbon-dominated ratio (C/O ≳ 1.0). We show that the spatial distribution and peculiar line kinematics of both CS and SO molecules can be well explained by azimuthal variations in the C/O ratio. We propose a shadowing mechanism that could lead to such a chemical dichotomy. Our results imply that tracing the formation history of giant exoplanets using their atmospheric C/O ratios will need to take into account time-dependent azimuthal C/O variations in a planet's accretion zone.

Facilities such as the James Webb Space Telescope and the European Space Agency's upcoming Ariel mission are opening a new era of exoplanetary studies, promising to characterize the atmospheric composition of over 1,000 worlds by the early 2030s. Such observations provide exciting opportunities to constrain planetary formation and evolution models. To enable this science, we must understand the chemical budget of planetary nurseries.

Of particular importance are carbon and oxygen, which are among the most abundant volatile elements, and prominent in both protoplanetary disk and planetary chemistry. The elemental carbon-to-oxygen ratio (C/O) is a potential formation tracer, linking the volatile composition of an exoplanet atmosphere directly to the disk region in which it was accreted[1–3]. The classical view of the C/O ratio in disk gas or solids is that of a multistep function, with jumps at the snowlines of dominant molecular species[4]. Considering dust growth and drift, vapour diffusion, refractory carbon destruction, chemical kinetics and planetesimal and disk evolution adds substantial complexity, but the fundamental conclusion remains that the planetary C/O ratio is related to its formation history[5–15].

Empirical findings based on spectroscopic observations support the hypothesis that the gas-phase elemental C and O abundances can vary both with radial location in a disk and between different disks[16–22]. While determining the precise C/O ratio in planet-forming gas is generally not simple, distinguishing between oxygen- or carbon-dominated chemistry (C/O < 1 or C/O ≳ 1, respectively) is more feasible. The two chemical regimes are characterized by entirely

[1]Department of Physics and Astronomy, University College London, London, UK. [2]Tartu Observatory, Tõravere, Estonia. [3]Leiden Observatory, Leiden University, Leiden, the Netherlands. [4]Department of Astronomy, University of Michigan, Ann Arbor, MI, USA. [5]Department of Astronomy, University of Virginia, Charlottesville, VA, USA. [6]Max-Planck Institut für Extraterrestrische Physik (MPE), Garching, Germany. [7]Center for Space and Habitability, Universität Bern, Bern, Switzerland. [8]National Astronomical Observatory of Japan, Mitaka, Japan. [9]Department of Earth Sciences and Institute of Astronomy, University of Cambridge, Cambridge, UK. [10]School of Physics and Astronomy, University of Leeds, Leeds, UK. e-mail: luke.keyte.18@ucl.ac.uk

https://doi.org/10.1038/s41550-023-01951-9

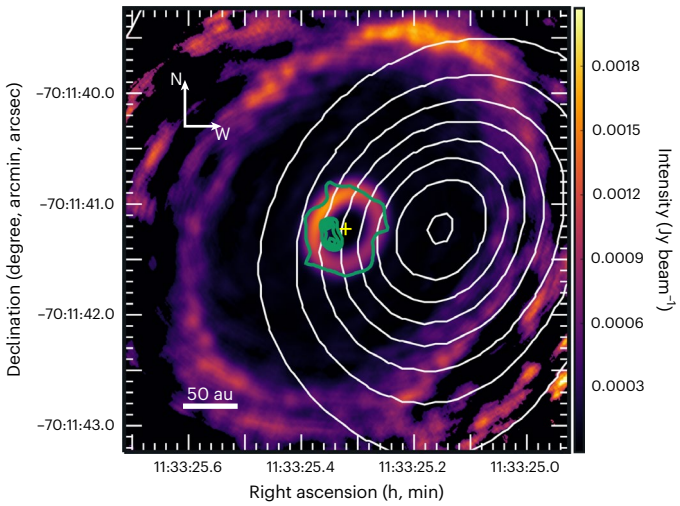

Fig. 1 | Azimuthal disparity of SO and CS emission. ALMA 870 μm continuum emission map[32], overlaid with SO 7_7–6_6 and 7_8–6_7 emission contours (green) and CS 7–6 emission contours (white). The continuum emission has been scaled by r^3 to highlight emission in the outer disk. Contours are logarithmically spaced between 1σ and the peak flux. The position of the star is denoted by the yellow cross. Beam sizes are ~0.18″/20 au (SO) and ~4.78″/525 au (CS).

different compositions. The C_2H molecule is a powerful C/O tracer, strong C_2H emission being a beacon of C/O ≥ 1 in the disk gas due to the orders-of-magnitude increase in the abundance of hydrocarbons when excess carbon is available[6,12,23,24]. Another probe is the carbon-monosulfide-to-sulfur-monoxide molecular ratio (CS/SO), which varies by up to four orders of magnitude for small variations in the C/O ratio[25,26], and has led to claims of C/O > 1 in at least six disks[12,27,28]. Such results are usually disk-averaged (that is, unresolved) or indicative of radial variations in the gas composition. Until now, combined observations of CS and SO have not been made in any disk, so it has not been possible to fully utilize the diagnostic power of the CS/SO ratio in cases of asymmetric emission.

In this Article, using observations of both CS and SO, we present a remarkable azimuthal C/O variation in the planet-forming disk around HD 100546.

Results

Data and observational findings

We present a new detection of CS in HD 100546, alongside Atacama Large Millimeter/submillimeter Array (ALMA) SO observations first presented in ref. 29 (Figs. 1 and 2). HD 100546 is a well-studied 2.49 ± 0.02 $M_\odot$ Herbig Be star, with an estimated age of ~5 Myr (ref. 30), and distance of 110 ± 1 pc. The star hosts a bright disk with a central dust cavity out to 13 au and another dust gap between $r \approx 40$ au and $r \approx 150$ au (where r is the radial distance from the star), bounded on both sides by dust rings[31,32]. Multiple observations provide evidence for at least two planetary candidates within the disk at $r \approx 13$ au and $r \approx 55$ au (refs. 31,33–35).

CS is detected at 9σ confidence (0.90 ± 0.10 Jy beam^{-1} km s^{-1} at emission peak, as measured from the integrated intensity map), using the Atacama Compact Array (ACA) in Cycle 4 (Fig. 2, top right). The emission is essentially unresolved, as the beam size (4.78″) is almost equal to the radial extent of the gas disk, as traced by CO[36]. Fitting a Gaussian, we find the peak of the CS emission to be considerably offset from the host star by ~1″. We confirm that the offset is related to a physical characteristic of the source, rather than a pointing error (Supplementary Discussion 1 and Supplementary Fig. 1). We determine the radial separation between the peak of the emission and the host star by exploiting the known inclination and position angle of the disk to deproject the image, finding the emission peak to be radially offset ~100 au from the source.

We complement the new CS detection with high-resolution Cycle 7 observations of SO, first presented in ref. 29 (Fig. 2, top left). The emission primarily emanates from the inner dust cavity and the inside edge of the dust ring ($r \approx 13$ au), showing a clear azimuthal brightness asymmetry, where emission from the eastern side of the disk is a factor of ~2 brighter than from the western side.

The distinct morphologies of the SO and CS emission are mirrored in their respective spectral lines (Fig. 3), which have unusual and disparate velocity profiles. The SO line is broad (FWZI ≈ 15 km s^{-1}) and asymmetric, with a prominent blueshifted Keplerian peak at about −7.5 km s^{-1}. In contrast, the CS emission is narrower (FWZI (full width at zero intensity) ≈ 10 km s^{-1}) and sharply peaked in the red (about +1.5 km s^{-1}).

In summary, the CS and SO emission show clear azimuthal asymmetries in their spatial morphologies, and peculiar spectral line profiles. It is striking that emission from each of these species appears to emanate from distinct and opposite azimuthal regions of the disk. We argue that these features can be fully explained by chemistry resulting from azimuthal C/O variations in the disk.

Modelling

To investigate the origin of the spatial and spectral asymmetries in the CS and SO emission, we ran source-specific models using the two-dimensional physical-chemical code DALI[37,38]. The disk chemical composition is obtained from a chemical network simulation, in which the gas-grain chemistry is solved time dependently. Our model uses a geometry outlined in Fig. 4, in which the disk is composed of two chemically distinct regions. The majority of the disk has a composition consistent with previous studies of HD 100546, in which C/O = 0.5 (ref. 39). We vary the composition in a small angular region of the disk, such that C/O is elevated within an azimuthally localized ‘wedge’ (C/O > 1), dictated by variations in the gas-phase H_2O, CO and atomic O abundances (Supplementary Discussion 2 and Supplementary Fig. 2).

We explored a wide parameter space, taking into account a range of wedge sizes and azimuthal locations, carbon and oxygen abundances, and chemical timescales. The model presented here incorporates a high-C/O wedge extending azimuthally 60°, centred 10° north of west. Modelled integrated intensity maps for both the CS 7–6 and stacked SO 7_7–6_6 and 7_8–6_7 emission are presented in Fig. 2 (bottom row). Our model reproduces the CS emission morphology well. The emission peak is considerably offset towards the west (~75 au deprojected), with a peak flux that matches the observation within a factor of ~1.1. The brightness asymmetry in the SO emission is also reproduced by our model, peaking towards the southwest at a radial separation of ~20 au. The peak flux matches the observations within a factor of ~1.2. A more refined model may be needed to fully reproduce the SO brightness distribution, although we note that the precise distribution can vary depending on the parameters used in the imaging during the data reduction[29]. The east/west asymmetry is always maintained, and is the key feature reproduced by our model.

The modelled spectral lines are shown in Fig. 3. The modelled CS line profile includes a prominent narrow single peak, redshifted ~2 km s^{-1} from the source velocity, matching the observation to within ~0.5 km s^{-1}. While it is possible to match the peak location more precisely by changing the orientation of the high-C/O wedge, this results in a slightly lower peak flux (Extended Data Fig. 2). The modelled SO line profile reproduces both the double-peaked structure and the peak flux value. The linewidth is a close match to the observation, where the flux density in the blueshifted component is ~1.7 times greater than that of the redshifted component.

Modelled CS and SO abundance maps are presented in Extended Data Fig. 1. We note that our model predicts that the bulk of the SO emission emanates from the dust ring just outside the cavity, whereas

https://doi.org/10.1038/s41550-023-01951-9

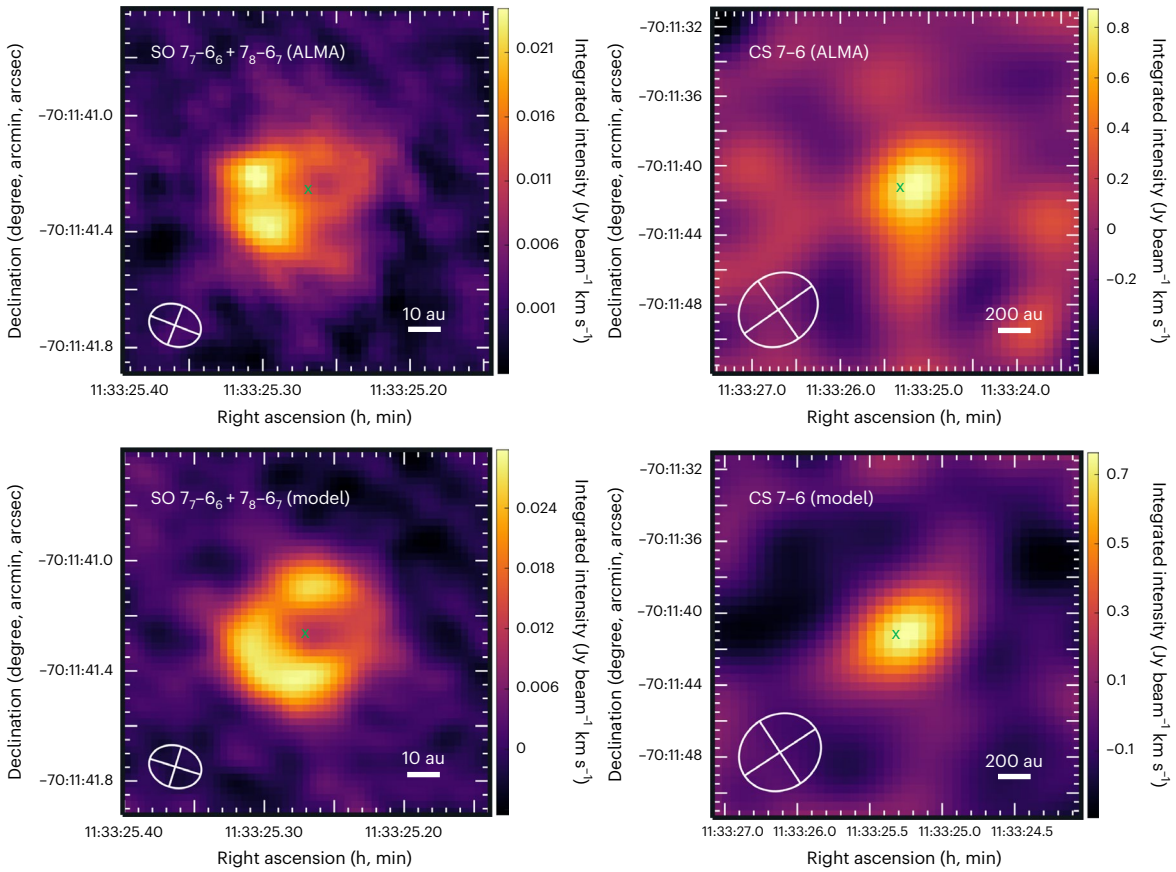

Fig. 2 | Detected and modelled SO and CS emission in HD 100546. Top left: integrated intensity map of the stacked SO 7$_7$–6$_6$ and 7$_8$–6$_7$ transitions observed with the ALMA[29]. Top right: integrated intensity map of the CS 7–6 transition observed with the ACA, with a 1σ clip. Bottom left: modelled stacked SO 7$_7$–6$_6$ and 7$_8$–6$_7$ integrated intensity map. Bottom right: modelled CS 7–6 integrated intensity map. The position of the star is indicated with the green cross. The synthesized beam size is indicated by the white ellipse in the lower left corners.

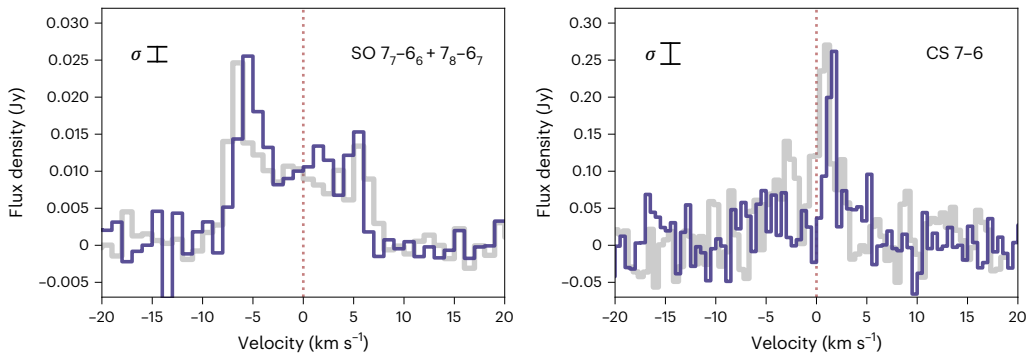

Fig. 3 | Spectral line profiles. Left: observed stacked SO 7$_7$–6$_6$ and 7$_8$–6$_7$ spectrum extracted using a 0.6'' elliptical mask (grey) and model (blue). Right: observed CS 7–6 spectrum extracted using a 5'' elliptical mask smoothed by the beam (grey) and model (blue). Line profile velocities have been corrected for the source velocity (V_{LSRK} = 5.7 km s^{-1}).

ref. 29 used the line kinematics to infer that it originates primarily from within the cavity itself. One possible explanation is that our model lacks a smooth transition between the cavity and dust ring, instead having a sharp boundary. In addition, the inclination and stellar mass used in our model differs from the values reported in ref. 29. Literature values vary between i = 32° and i = 44° (where i is the inclination) (refs. 31,40) and between M_* = 2.2 $M_\odot$ and M_* = 2.5 $M_\odot$ (where M_* is the mass of the star)(refs. 30,40,41), which can result in variations of the predicted inner edge of the SO emission (~9–18 au).

Discussion

We have shown that the emission from CS and SO in the HD 100546 protoplanetary disk can be well reproduced by a chemical model that incorporates an azimuthal C/O variation. This adds a new dimension of complexity to the relationship between C/O in disks and their planetary progeny. We now aim to understand the origin of this novel type of chemical dichotomy.

The depletion of volatile elemental carbon and oxygen is ubiquitous in protoplanetary disks around both T Tauri and Herbig Ae/

https://doi.org/10.1038/s41550-023-01951-9

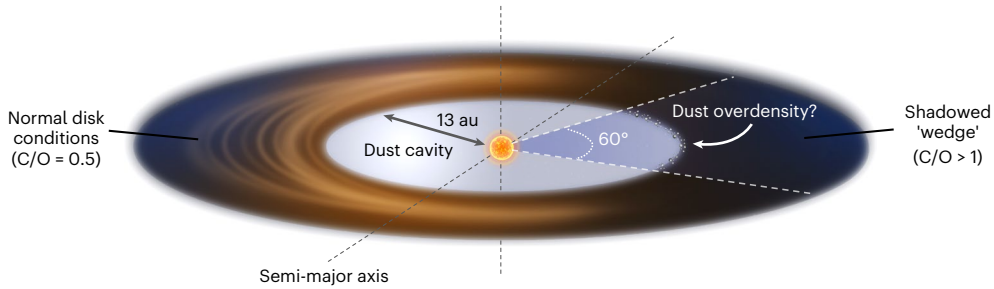

Fig. 4 | Geometry of the HD 100546 disk model. The disk is composed of two chemically distinct regions; the majority of the disk has C/O = 0.5, apart from a 60° arc where C/O > 1. We propose that an overdensity of dust, associated with a newly forming planet within the cavity, casts a shadow over an azimuthally localized region of the disk. This results in lower temperatures, which causes additional H_2O freeze-out, leading to an elevated gas-phase C/O ratio. Note that this schematic is not to scale; the gas disk extends out to ~500 au.

Be stars. For instance, disks around AS 209, MWC 480 and HD 163296 all exhibit substellar C/H and O/H ratios[12]. Oxygen is typically more depleted than carbon due to its removal from the disk atmosphere through the freezing-out of water onto large dust grains, resulting in elevated C/O ratios (~2). However, our modelling of HD 100546 finds no evidence of substantial oxygen depletion relative to carbon in this disk, with a best-fit disk-averaged C/O ratio of <1. The majority of the disk is warm enough to preclude freeze-out of CO and CO_2 (Extended Data Fig. 3), and water loss through freeze-out onto large grains is tempered by the presence of a dust cavity where large grains are heavily depleted (small grains are not as important for permanent freeze-out, as they cycle vertically within the disk due to turbulence, releasing their ices upon each return to the disk atmosphere). Photodesorption also limits the extent of the water snow surface (Fig. 5). Analysis of water emission from HD 100546 reveals that a high H_2O abundance in the photodesorption region is necessary to match observations, with line kinematics indicating that the emission extends out to $r \approx 300$ au (refs. 42,43). Therefore, we expect the majority of the HD 100546 disk to have a gas-phase C/O ratio closer to 0.5, and attribute the observed asymmetries to a region of elevated C/O localized in azimuth.

The main feature we have identified is an azimuthally confined zone of elevated CS abundance, coincident with a region of depleted SO, which we ascribe to a local enhancement in the C/O ratio (>1). How could this come about? Asymmetries in the structure of both dust and gas are common in protoplanetary disks, particularly transition disks like HD 100546 that have large central cavities[44]. Dust asymmetries are often attributed to the trapping of millimetre-sized grains in vortices formed by the Rossby wave instability[45], induced by a planetary companion. Vortices can also form through various hydrodynamical instabilities, or at the edges of low-viscosity 'dead zones'. In recent years, high-resolution ALMA observations have enabled comparisons between dust asymmetries and molecular gas at small scales. While several studies have drawn tentative links[46–51], there is often no clear connection to be made. Furthermore, asymmetries observed in a particular species are often not observed in other species or transitions of the same species within the same disk. The physical mechanisms responsible for gas asymmetries cannot therefore be easily attributed to vortices.

In HD 100546, gas-phase asymmetries have previously been observed in a range of molecular species, including various CO transitions (for example, refs. 39,52,53), OH (ref. 54) and SO (ref. 7). These have often been attributed to temperature variations that are thought to result from obscuration by a warped inner dust disk[36,52], such that one side of the disk is 10–20 K cooler than the other. Disk warps have been shown to produce azimuthal temperature variations, even in the absence of a shadowing inner disk[55]. In such a scenario, an azimuthal variation in the temperature structure could have a notable impact on the disk chemistry, resulting in azimuthal variations in molecular

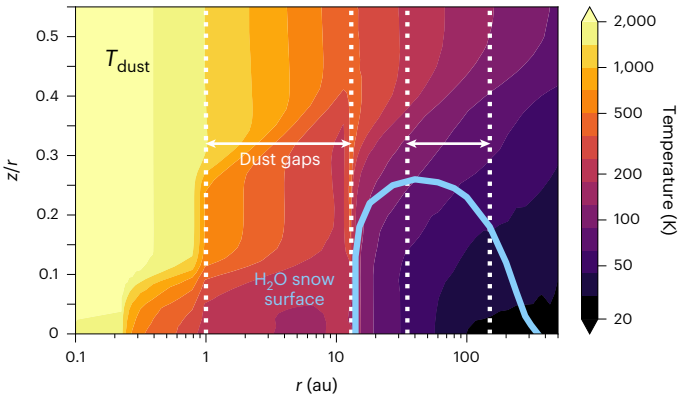

Fig. 5 | HD 100546 model dust temperature map. Most of the disk is warm enough to preclude freeze-out of CO and CO_2. The H_2O snow surface (blue line) largely coincides with a dust gap in the outer disk (white dotted lines). Millimetre-sized grains are highly depleted in this region, removing grain surface area available for permanent H_2O freeze-out. The outer edge of the snow surface is curtailed by photodesorption. T_{dust} is the dust temperature in Kelvin and z is the vertical height of the disk in au.

abundances[56]. However, near-infrared observations at small spatial scales (~1 au) find no evidence supporting an inclined inner dust disk ($r < 1$ au)[57–60], which may indicate that the structure of the gas and dust is different within the inner few au. Currently, no physical mechanism is known to cause such decoupling between the gas and small dust grains, suggesting that another process might be at play.

An alternative scenario is that asymmetric emission is connected to ongoing planet formation within the inner cavity of HD 100546. Reference [29] proposed that the observed SO asymmetry may be tracing shocked gas in the vicinity of a circumplanetary disk. Indeed, the peak of the observed SO emission is cospatial with the location of a protoplanet candidate inferred from scattered light images[34] and excess CO emission[61]. Comparing Cycle 7 and Cycle 0 spectra of SO emission provides further evidence of a newly forming planet, as the shift in emission peak is consistent with a hotspot of molecular gas in orbital rotation within the inner cavity[7,29]. Our findings do not rule out this possibility. While our model can be modified to account for an additional component of SO emission related to a circumplanetary disk (CPD), a CPD alone is not able to account for the asymmetries observed for both SO and CS. Both the kinematics and the spatially resolved SO emission are consistent with a Keplerian protoplanetary disk. The spatial distribution of the emission indicates that any contribution from a CPD to the total SO flux would be relatively small.

https://doi.org/10.1038/s41550-023-01951-9

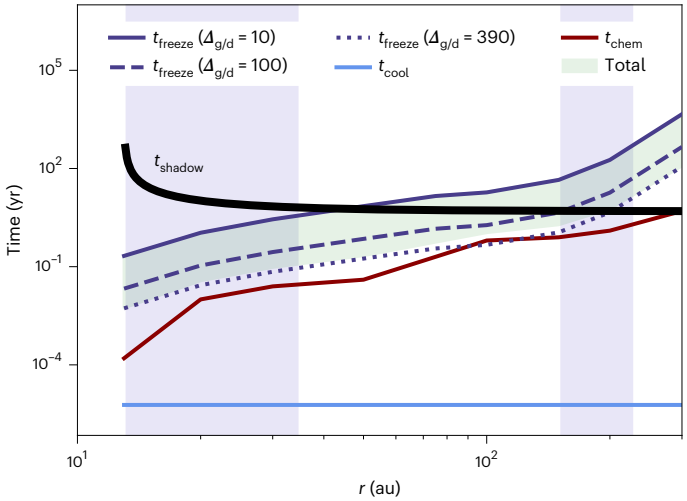

Fig. 6 | Cooling, freeze-out and chemical timescales. The maximum time available for the combination of cooling, freeze-out and shadowing to occur is dictated by the period a specific region of the disk remains in shadow, which is related to the orbital period of the shadowing material (black line). The cooling timescale is denoted in light blue, freeze-out timescale in dark blue (for a range of $\Delta_{g/d}$) and chemical timescale in red. The green shaded area represents the sum total of these timescales within the range of considered $\Delta_{g/d}$, which follows the freeze-out timescale as the cooling and chemical timescales are negligible. Purple shaded regions denote location of millimetre dust rings.

This leads us to propose an alternative explanation, consistent with an azimuthal C/O variation. We suggest that an overdensity of dust associated with the inner protoplanet casts a shadow on an azimuthally localized region of the outer disk. This causes dust temperatures in the disk atmosphere to decrease, which leads to additional H_2O freeze-out on grain surfaces. In turn, this locks a considerable fraction of gas-phase oxygen into ices, causing the local gas-phase C/O ratio to become super-solar. As the disk chemistry rebalances, SO is rapidly destroyed while CS is rapidly formed, on timescales shorter than the shadow transit time.

Falsifying this hypothesis using past observations is not straightforward. Our understanding of dust substructures within HD 100546 is shaped by both infrared and (sub)millimetre observations, which contain many features. These include spiral arms, dark and bright azimuthal wedges, emission hotspots[57,62], and an inner ring sculpted by a maze of ridges and trenches[32,63]. We note that the location of the protoplanet within the inner cavity of HD 100546 is not coincident with our high-C/O wedge towards the west, but closer to the region of bright SO emission. Nevertheless, material associated with a forming planet can be highly azimuthally and vertically extended[64]. Indeed, several features suggestive of shadowing have been identified on the western side of the disk. The most prominent is a dark region towards the northwest, already linked to a possible large-scale shadow[57]. This region covers a similar azimuthal width to the high-C/O wedge used in our model, and overlaps with it considerably (the local minimum in the azimuthal brightness profile is orientated slightly farther northwest by ~10°). At least one other similar dark wedge was identified on the opposite side of the disk[65]. Other features that could be related to a dust overdensity include a horseshoe-like structure identified in 7 mm observations at the inner southwest edge[66], and a bar-like structure seen in Hα polarized light, which may be a 'streamer' of dust dragged in by gas flowing from the outer to inner disk[67]. However, it is unclear whether such features could lead to large-scale shadowing. So, while HD 100546 clearly shows a number of morphological features that could be related to shadowing, linking any such feature to the region of high-C/O identified here remains open to interpretation.

To determine whether a shadow could cause the required chemical changes to produce C/O > 1, we examined three timescales: cooling, freeze-out and chemical conversion (Supplementary Discussion 2). As the shadow falls on part of the disk, the dust must cool enough for H_2O to freeze-out. Kinetics will then funnel O from other reservoirs (atomic O, CO) into the water-ice sink, eventually elevating the CS abundance and depleting SO within the shadowed region. The combined time needed for these processes to operate must be shorter than the time spent in shadow, which converges to ~5 yr in the outer disk (based on model parameters). Considering a range physical conditions from our model in the CS-emitting region (Extended Data Fig. 1), we find that the C/O ratio can exceed unity in ≤5 yr inside of $r \lesssim 200$ au. These results are illustrated in Fig. 6. The shadowing hypothesis can be tested in the near future with high-resolution observations of the CS emission, to establish whether the feature moves. Moving shadows of this nature have already been observed in other disks such as TW Hya[68].

Regardless of the precise mechanisms that lead to azimuthal C/O variations in the HD 100546 disk, it is clear that such a chemical dichotomy will have a profound impact on the final composition of planets forming within it. Growing planets are supplied by gas and dust from their surroundings. Planets that move in and out of two chemically distinct regions during the course of their evolution can be expected to have chemically complex envelopes, formed of material accreted from both regions. The degree to which envelope composition mirrors that of either region in the disk will be governed by complex chemical and physical processes. If shadowing is indeed responsible for the azimuthal C/O variation, we may expect its effect on planetary composition to be even more profound in warm disks such as HD 100546, where there is a higher fraction of gas-phase water available for freeze-out.

The results presented here therefore add a new consideration to the way in which we interpret observations and model gas-phase asymmetries in protoplanetary disks. The classical view of a radially varying C/O ratio must be readdressed if we are to draw meaningful links between the composition of exoplanet atmospheres and the disks in which they form. Determining the C/O ratio at small spatial scales must be a major goal of future observations, if we are to build models that can meaningfully predict planetary formation pathways.

Methods

Data reduction

HD 100546 was observed with the ACA in Band 7 during Cycle 4, in two separate execution blocks on 14 November and 24 November 2016 (programme 2016.1.01339.S; principal investigator M. Kama). The observations cover eight molecular rotational transitions of seven sulfur-bearing species/isotopologues, outlined in Supplementary Table 1. Eight scans were performed for a total on-source time of 50.64 min, with baselines ranging from 8 m to 45 m. System temperatures varied from 103 K to 170 K and the average precipitable water vapour was 1.0 mm. J1058+0133 was used as both the bandpass and the flux calibrator, while J1147−6753 was used as the phase calibrator.

The data reduction was completed using the ALMA Pipeline in the Common Astronomy Software Package (CASA) version 5.6.1-8. Self-calibration was performed but found to have marginal impact due to low signal-to-noise ratio (S/N) of the data. Continuum and line imaging were performed with the tCLEAN algorithm using natural weighting to maximize the S/N ratio of the data. The resulting synthesized beam size was ~4.78″ × 4.06″, with slight variations depending on the spectral window. We used a cell size of 0.5″ to ensure that the beam is well sampled. Continuum subtraction was performed with the CASA task uvcontsub, using a single-order polynomial fit to the line free channels. The spectral resolution, bandwidth and synthesized beam size for each of the transitions are listed in Supplementary Table 1.

CS 7–6 at 342.883 GHz is successfully detected, while all other transitions are undetected. The CS 7–6 integrated intensity map (Fig. 2, top right) was generated from a 20″ × 20″ region centred on the source,

where the integrated intensity is determined between −14.5 km s^{-1} and 25.5 km s^{-1}, corresponding to channels expected to contain emission (about ±20 km s^{-1} from the source velocity V_{LSRK} = 5.7 km s^{-1}, where LSRK is the kinematic local standard of rest). The detection is made at a 9σ confidence level, with a peak flux of 0.90 Jy beam^{-1} km s^{-1}, and a root mean square of 0.10 Jy beam^{-1} km s^{-1} as measured from the emission-free regions of the integrated intensity map. Channel maps are presented in Supplementary Fig. 3, from which we measure a peak flux density of 0.21 Jy beam^{-1} and a root mean square of 0.024 Jy beam^{-1}.

We extracted the spectrum from the CLEAN cube using an elliptical aperture with a 5.0″ radius centred on the source (approximately the same size as the disk as traced by ^{12}CO emission[31]), where the edges of the mask were smoothed by the beam. We also extracted a spectrum using a Keplerian mask (https://github.com/richteague/keplerian_mask), which excludes noisy pixels that are not directly associated with emission from a disk in Keplerian rotation. The mask identifies which pixels in the image cubes have Doppler-shifted line velocities that match the Keplerian velocity, based on the velocity profile of a disk rotating around a star of mass $M_\odot$ = 2.4 $M_\odot$. Pixels with velocities that do not match the Keplerian velocity are masked. The mask is convolved with a beam of equal size to the observation, to provide a buffer between the mask edge and emission edge. The total disk-integrated flux was extracted using the CASA task specflux, and determined to be 0.62 Jy km s^{-1} for the Keplerian-masked cube, where the mask was cut at ±4 km s^{-1} either side of the source velocity to remove noisy channels. The disk-integrated flux extracted from the elliptically masked cube was 1.02 Jy km s^{-1}. Due to the peculiar nature of the CS line profile, our analysis utilizes only the elliptically masked spectrum, to not mistakenly remove any real emission.

We employed a number of techniques in an attempt to extract weak spectral signatures from the remaining spectral windows centred on other molecular species (Supplementary Table 1). We began by extracting spectra from the CLEAN image cubes using an elliptical aperture with a 5.0″ radius centred on the source. Integrated intensity maps were created from the CLEAN cubes, which yielded no detections.

Next, we applied a Keplerian mask to each of the CLEAN image cubes to maximize the S/N ratio in the image plane. We extracted spectra and generated integrated intensity maps from the masked cubes, which again resulted in no detections. We also tried stacking the SO 2_1–1_0 and 8_8–7_7 lines in the image plane by adding together the integrated intensity maps and spectra. However, SO remained undetected.

Finally, we applied a matched filter to the visibility data, to maximize the S/N ratio in the u–v plane[69]. The matched filter technique utilizes a template image cube that samples the u–v space to obtain a set of template visibilities. These can then be used as a filter, which is cross-correlated with the data in an attempt to detect any weak emission. Matched filtering has previously been used to successfully detect weak spectral line features in HD 163296, TW Hya and HD 100546, providing an improvement in the S/N ratio of up to ~500% when compared with alternative techniques[69–71]. We created template emission profiles for each of the spectral windows in the ACA data by modelling the spectral line emission with the DALI thermo-chemical disk modelling code ('Dust and Lines', see 'Chemical modelling'). The matched filter was then run for each of the spectral lines individually, which again resulted in non-detections for all lines. We derived 3σ upper limits for the disk-integrated flux for each of the non-detected spectral lines, calculated from the elliptically masked integrated intensity maps (Supplementary Table 1).

We also report the serendipitous detection of C^{18}O 3–2 in the spectral window centred on SO 2_1–1_0 at 329.385 GHz. The detection is made at an ~24σ confidence level, with a peak flux of 7.2 ± 0.3 Jy beam^{-1} km s^{-1}, as measured from the integrated intensity map. The disk-integrated flux is measured using the procedure outlined above, determined to be 5.41 Jy km s^{-1} using a Keplerian mask, and 8.22 Jy km s^{-1} using an elliptical mask.

Complementary data

To complement our CS 7–6 data for HD 100546, we make use of a wide range of archival data. Of particular importance for this study are detections of SO 7_7–6_6 and SO 7_8–6_7 first presented in ref. 29 (ALMA programme 2019.1.00193.S; principal investigator A. S. Booth). We note that the maximum recoverable scale of the observations is 10.422″ (~1,150 au), which is much larger than the gas disk[31], and we therefore do not expect any flux missing on short spacings. Similarly, the maximum recoverable scale of our ACA observations is 21.266″ (~2,350 au), also much larger than the gas disk. The full list of line fluxes and upper limits used to constrain our model is presented in Supplementary Table 2.

Chemical modelling

To investigate the origin of the azimuthal asymmetries in various molecular species in the HD 100546 disk, we ran source-specific models using the two-dimensional physical-chemical code DALI[37,38]. The code begins with a parameterized gas and dust density distribution and an input stellar spectrum, then uses Monte Carlo radiative transfer to determine the ultraviolet radiation field and dust temperature. This provides an initial guess for the gas temperature, which begins an iterative process in which the gas-grain chemistry is solved time dependently. Finally, the ray-tracing module is used to obtain spectral image cubes, line profiles and disk-integrated line fluxes.

Disk parameters. The disk structure is fully parameterized, with a surface density that follows the standard form of a power law with an exponential taper:

$$\Sigma_{\rm gas} = \Sigma_{\rm c}\left(\frac{r}{R_{\rm c}}\right)^{-\gamma} \exp\left[-\left(\frac{r}{R_{\rm c}}\right)^{2-\gamma}\right] \quad (1)$$

where r is the radius, γ is the surface density exponent, $\Sigma_{\rm c}$ is some critical surface density and $R_{\rm c}$ is some critical radius, such that the surface density at $R_{\rm c}$ is $\Sigma_{\rm c}/e$ (where e is the base of the natural logarithm). The scale height is then given by:

$$h(r) = h_{\rm c}\left(\frac{r}{R_{\rm c}}\right)^{\psi} \quad (2)$$

where $h_{\rm c}$ is the scale height at $R_{\rm c}$, and the power-law index of the scale height, ψ, describes the flaring structure of the disk.

$\Sigma_{\rm gas}$ and $\Sigma_{\rm dust}$ extend from the dust sublimation radius ($R_{\rm sub}$) to the edge of the disk ($R_{\rm out}$), and can be varied independently inside the cavity radius $R_{\rm cav}$ with the multiplication factors $\delta_{\rm gas}$ and $\delta_{\rm dust}$.

The gas-to-dust ratio is denoted $\Delta_{\rm g/d}$. Dust settling is implemented by considering two different populations of grains; small grains (0.005–1 μm) and large grains (0.005–1 mm). The vertical density structure of the dust is such that large grains are settled towards the midplane, prescribed by the settling parameter χ:

$$\rho_{\rm dust,large} = \frac{f\Sigma_{\rm dust}}{\sqrt{2\pi}r\chi h} \exp\left[-\frac{1}{2}\left(\frac{\pi/2-\theta}{\chi h}\right)^2\right] \quad (3)$$

$$\rho_{\rm dust,small} = \frac{(1-f)\Sigma_{\rm dust}}{\sqrt{2\pi}rh} \exp\left[-\frac{1}{2}\left(\frac{\pi/2-\theta}{h}\right)^2\right] \quad (4)$$

where f is the mass fraction of large grains and θ is the opening angle from the midplane as viewed from the central star. The physical disk parameters used in our model are given in Supplementary Table 3.

Stellar parameters. HD 100546 is a well-studied 2.49 ± 0.02 $M_\odot$ Herbig Be star of spectral type B9V, with an estimated age of ~5 Myr (ref. 30). The star is noted for its proximity, located at a distance of 110 ± 1 pc (ref. 72). We note that this differs non-trivially from previous estimates of

97 ± 4 pc from Hipparcos. The stellar spectrum was modelled by ref. 37 using dereddened FUSE (far ultraviolet spectroscopic explorer) and IUE (international ultraviolet explorer) observations at ultraviolet wavelengths, and then extended to longer wavelengths using the B9V template of ref. 73. The stellar luminosity is 36 $L_\odot$ (ref. 39).

Chemical network. The chemical network used in our model is based on a subset of the UMIST (University of Manchester Institute of Science and Technology) 06[74] network. It consists of 122 species (including neutral and charged polycyclic aromatic hydrocarbons) and 1,701 individual reactions. The code includes H_2 formation on dust, freeze-out, thermal and non-thermal desorption, hydrogenation, gas-phase reactions, photodissociation and photoionization, X-ray induced processes, cosmic-ray induced reactions, polycyclic aromatic hydrocarbon/small grain charge exchange/hydrogenation, and reactions with vibrationally excited H_2. For grain surface chemistry, only hydrogenation of simple species is considered (C, CH, CH_2, CH_3, N, NH, NH_2, O and OH). The details of these processes are described more fully in ref. 37. Of particular relevance to this study, the network includes reactions for 30 sulfur-bearing species, including all those listed in Supplementary Table 1. Model parameters of relevance to the disk chemistry are listed in Supplementary Table 3.

Basic fitting procedure. Our fitting process follows the procedure outlined in ref. 39, making use of additional observational constraints and a larger grid of models. We begin by fitting the spectral energy distribution using a grid of 1,728 models, in which the parameters R_{gap}, ψ, h_c, δ_{dust} and $\Delta_{g/d}$ are varied. At this stage, Σ_{gas} is kept fixed at an arbitrary value such that changes to $\Delta_{g/d}$ are equivalent to changes only in the dust mass, thus providing us with a baseline estimate for the total dust mass. We find a best-fit total dust mass of $1.12 \times 10^{-3}\,M_\odot$, consistent with previous studies[39].

Next, we use the upper limits of the HD 56 μm and 112 μm lines to constrain the maximum gas mass. A second grid of models is run in which Σ_{gas} and $\Delta_{g/d}$ are varied in lockstep, allowing the gas mass to vary while maintaining the best-fit dust mass. We constrain the total gas mass to $<5.6 \times 10^{-1}\,M_\odot$, equivalent to a gas-to-dust ratio of $\Delta_{g/d} \approx 390$ (taking into account dust depletion in the inner cavity). This is not a tight enough constraint to uniquely determine the gas-to-dust ratio, so from this point on we adopt the interstellar value of $\Delta_{g/d} = 100$, equivalent to a total gas mass of $1.45 \times 10^{-1}\,M_\odot$. Our model allows for variations in $\Delta_{g/d}$ within the inner dust cavity, but does not take into account other radial variations such as the observed dust gap in the outer disk between $r \approx 40$ au and $r \approx -150$ au.

$[C]/[H]_{gas}$ and $[O]/[H]_{gas}$ are constrained by modelling the CO ladder, the line profiles of the CO 3–2, CO 6–5 and [C I] transitions, and the radial profile of the CO 3–2 emission from ref. 31. We find a best-fit oxygen abundance of $[O/H]_{gas} \approx (1\text{–}7) \times 10^{-5}$. When $[O/H]_{gas} > 7 \times 10^{-5}$, the [C I] line is underpredicted or the CO ladder is overpredicted, depending on $[C/H]_{gas}$. When $[O/H]_{gas} < 1 \times 10^{-5}$, the CO ladder is underpredicted for all values of $[C/H]_{gas}$. Adopting a fiducial oxygen abundance of $[O/H]_{gas} = 2 \times 10^{-5}$, we find $[C/H]_{gas} \approx (1\text{–}2) \times 10^{-5}$. C_2H upper limits presented in ref. 39 constrain the global C/O $\lesssim 1$, and we adopt $[C/H]_{gas} = 1 \times 10^{-5}$ for our fiducial model, giving a C/O ratio of 0.5. These values are consistent with those found in previous studies of HD 100546 (for example, ref. 39). As with that study, the main uncertainties are due to the limited constraints on the gas-to-dust ratio.

Finally, we constrain the gas-phase elemental sulfur abundance using the disk-integrated CS 7–6, SO 7_7–6_6 and SO 7_8–6_7 fluxes and radial intensity profiles, and upper limits for other sulfur-bearing species listed in Supplementary Table 1. For this study, we adopt a radially varying sulfur abundance profile, in which $[S/H] = 10^{-9}$ between 13 au and 30 au and $[S/H] = 10^{-8}$ between 150 au and 230 au, coincident with prominent millimetre dust rings. Outside of these regions, the sulfur is further heavily depleted by a factor of 1,000. This is based on high-resolution SO observations that suggest some level of correlation between SO emission and dust ring location[29]. If a single sulfur abundance is used for the entire disk, our model overpredicts SO emission from the outer dust cavity. A detailed study into the volatile sulfur abundance in HD 100546 is the focus of an upcoming companion paper (manuscript in preparation).

Modelling azimuthal asymmetries. We hypothesize that the asymmetries in the observed CS and SO emission can be explained by notable azimuthal variations in the elemental carbon and/or oxygen abundances in HD 100546. In such a scenario, the resulting chemistry leads to an azimuthal disparity in the production of carbon- and oxygen-bearing species.

Our aim is to produce a model in which oxygen-based chemistry dominates in one region of the disk, while carbon-based chemistry dominates in another region of the disk. We investigate whether such a model, using time-dependant chemistry, can self-consistently reproduce the asymmetry in the CS and SO emission.

We simplify our assumptions about the chemistry by constructing a model in which the disk consists of two distinct spatial regions. DALI is a two-dimensional code that relies on azimuthal symmetry to produce three-dimensional outputs, so to simulate azimuthal asymmetries it is necessary to run two separate models and splice together the outputs using the following procedure.

Our starting point is the full-disk model outlined in the previous section, where C/O = 0.5 ('model A'). Using the ray-tracing module in DALI, we obtain spectral image cubes for each transition, with the velocity resolution set to match the observations. Next, we run a second full-disk model in which the carbon and/or oxygen abundances are varied, such that the resulting C/O ratio is different from the first model ('model B'). Using a custom Python script, for each transition the spectral cube from model B is spliced together with its counterpart from model A, following the geometry outlined in Fig. 4. The resulting cube consists of a large 'crescent' region taken from model A, in which the C/O ratio is 0.5, and a smaller 'wedge' region extracted from model B, with a different C/O ratio. The size of the wedge is prescribed by the angle θ, and the orientation by the angle ϕ (measured from the centre of the wedge arc). Angles are measured in the plane of the cube, that is, they are not projected on to the disk, and as such do not directly correlate to angles measured in the disk plane. The result is that the angular region from which the wedge is extracted cuts through very slightly different azimuthal regions for different vertical positions within the disk. A more sophisticated model could take the vertical disk structure into account, but we expect the overall effect on the intensity maps and line profiles to be negligible. We note that that there is precedent in the literature for this kind of chemical modelling[75]. We process the model cubes using the CASA tasks simobserve and simanalyze to create simulated ALMA observations, using parameters that match the observations. Spectra are extracted and the cubes are then collapsed to generate moment-zero integrated intensity maps.

We explored a wide parameter space, considering large-scale variations in the carbon/oxygen abundance, wedge size and position, and chemical timescale. Our model grid covers elemental carbon and oxygen abundances that range from 1.0×10^{-6} to 2×10^{-4}, and C/O between 0.3 and 3.0 (~570 models in total). The angular size and position from which we extracted the wedge used parameters that varied from $\theta = 10°$ to $\theta = 90°$ and from $\phi = 0°$ to $\phi = 180°$. Both the carbon/oxygen abundances and overall size of the wedge are largely constrained by the best-fit full-disk model outlined in the previous section; the vast majority of the total disk structure must conform to this model if the general fit is to be maintained. Thus, the wedge region cannot be too large, nor can the carbon/oxygen abundances vary too dramatically without largely affecting the overall model fit. While large wedge angles better produce the spatial morphology of the SO emission, they lead to disk-integrated CS fluxes that are too high. Smaller wedge angles

better reproduce the CS flux, but fail to reproduce the offset in the CS emission from the host star, and lead to SO emission that extends too far around the western side of the disk.

We simulate the effects of disk shadowing by using the output abundances from the C/O = 0.5 model as input abundances to the chemical network for the high-C/O wedge model, such that the chemical conditions at the beginning of shadowing are similar to that of the unshadowed region of the disk. Before running the chemical network, we decrease the input H_2O, CO and atomic O abundances by varying amounts to investigate a range of C/O ratios. The physical justification for depleting each of these species is discussed in Supplementary Discussion 1. Models are run for a range of chemical timescales, to assess how quickly the chemistry rebalances. This method allows us to constrain the CO depletion factor to $\lesssim$0.8, via comparison with the CO 6–5, CO 3–2 and [C I] 1–0 lines obtained with the Atacama Pathfinder Experiment telescope and previously presented in ref. 39 (Supplementary Fig. 4; the depletion factor is defined as the ratio of the new abundance to the initial abundance). The CO 6–5 line profile has a prominent asymmetry in which the blueshifted peak is ~1.25 times brighter than the redshifted peak. CO depletion factors higher than ~0.8 fail to reproduce any notable asymmetry. We test the effects of modelling a range of CO depletion factors between 0 and 0.8, while varying the level of atomic oxygen and H_2O depletion, to cover a range of C/O ratios. To investigate C/O ratios greater than unity, it is necessary to redistribute some of the carbon from the removed CO into other gas-phase species. In this case, we place the carbon into neutral atomic carbon, following ref. 6. The model presented here uses a CO depletion factor of 0.3, an atomic oxygen depletion factor of 0.3 and an H_2O depletion factor of 0 (that is, total removal), resulting in a gas-phase C/O ratio of 1.5. The model is run to a chemical age of 5 yr, based on the approximate shadow transit time (Supplementary Discussion 2). The full set of parameters used for the model presented in this study are listed in Supplementary Table 3. Using these values, we find that a wedge size of $\theta = 60°$ centred 10° north of west ($\phi = 10°$) accurately reproduces both the CS and SO emission morphology and line profiles.

Data availability

The data presented here are from the ALMA Cycle 4 programme 2016.1.01339.S (principal investigator M. Kama). The raw data are publicly available from the ALMA archive. The reduced data and final imaging products are available upon reasonable request from the corresponding author.

Code availability

The ALMA data were reduced using CASA version 5.6.1-8, which is available at https://casa.nrao.edu/. Outputs from the DALI physical-chemical disk models are available at https://doi.org/10.5281/zenodo.7734194.

References

1. Madhusudhan, N. C/O ratio as a dimension for characterizing exoplanetary atmopsheres. *Astrophys. J.* **758**, 36 (2012).
2. Cridland, A. J., Pudritz, R. E. & Alessi, M. Composition of early planetary atmospheres—I. Connecting disc astrochemistry to the formation of planetary atmospheres. *Mon. Not. R. Astron. Soc.* **461**, 3274–3295 (2016).
3. Mordasini, C., van Boekel, R., Mollière, P., Henning, T. & Benneke, B. The imprint of exoplanet formation history on observable present-day spectra of hot Jupiters. *Astrophys. J.* **832**, 41 (2016).
4. Oberg, K. I., Murray-Clay, R. & Bergin, E. A. The effects of snowlines on C/O in planetary atmospheres. *Astrophys. J. Lett.* **743**, L16 (2011).
5. Madhusudhan, N., Knutson, H., Fortney, J. J. & Barman, T. in *Protostars and Planets VI* (eds Beuther, H. et al.) 739–762 (University of Arizona Press, 2014).
6. Bergin, E. A. et al. Hydrocarbon emission rings in protoplanetary disks induced by dust evolution. *Astrophys. J.* **831**, 101 (2016).
7. Booth, R. A., Clarke, C. J., Madhusudhan, N. & Ilee, J. D. Chemical enrichment of giant planets and discs due to pebble drift. *Mon. Not. R. Astron. Soc.* **469**, 3994–4011 (2017).
8. Krijt, S., Schwarz, K. R., Bergin, E. A. & Ciesla, F. J. Transport of CO in protoplanetary disks: consequences of pebble formation, settling, and radial drift. *Astrophys. J.* **864**, 78 (2018).
9. Booth, R. A. & Ilee, J. D. Planet-forming material in a protoplanetary disc: the interplay between chemical evolution and pebble drift. *Mon. Not. R. Astron. Soc.* **487**, 3998–4011 (2019).
10. Cridland, A. J., Eistrup, C. & van Dishoeck, E. F. Connecting planet formation and astrochemistry. Refractory carbon depletion leading to super-stellar C/O in giant planetary atmospheres. *Astron. Astrophys.* **627**, A127 (2019).
11. van 't Hoff, M. L. R., Bergin, E. A., Jørgensen, J. K. & Blake, G. A. Carbon-grain sublimation: a new top-down component of protostellar chemistry. *Astrophys. J.* **897**, L38 (2020).
12. Bosman, A. D. et al. Molecules with ALMA at planet-forming scales (MAPS). VII. Substellar O/H and C/H and superstellar C/O in planet-feeding gas. *Astrophys. J. Suppl. Ser.* **257**, 7 (2021).
13. Turrini, D. et al. Tracing the formation history of giant planets in protoplanetary disks with carbon, oxygen, nitrogen, and sulfur. *Astrophys. J.* **909**, 40 (2021).
14. Van Clepper, E., Bergner, J., Bosman, A., Bergin, E. & Ciesla, F. Chemical feedback of pebble growth: impacts on CO depletion and C/O ratios. *Astrophys. J.* **927**, 206 (2022).
15. Hobbs, R., Shorttle, O. & Madhusudhan, N. Molecular tracers of planet formation in the atmospheres of hot Jupiters. *Mon. Not. R. Astron. Soc.* **516**, 1032–1046 (2022).
16. Favre, C., Cleeves, L. I., Bergin, E. A., Qi, C. & Blake, G. A. A significantly low CO abundance toward the TW Hya protoplanetary disk: a path to active carbon chemistry? *Astrophys. J. Lett.* **776**, L38 (2013).
17. Qi, C. et al. Imaging of the CO snow line in a solar nebula analog. *Science* **341**, 630–632 (2013).
18. van der Marel, N. et al. Resolved gas cavities in transitional disks inferred from CO isotopologs with ALMA. *Astron. Astrophys.* **585**, A58 (2016).
19. Du, F. et al. Survey of cold water lines in protoplanetary disks: indications of systematic volatile depletion. *Astrophys. J.* **842**, 98 (2017).
20. Cleeves, L. I. et al. Constraining gas-phase carbon, oxygen, and nitrogen in the IM lup protoplanetary disk. *Astrophys. J.* **865**, 155 (2018).
21. Zhang, K., Bergin, E. A., Schwarz, K., Krijt, S. & Ciesla, F. Systematic variations of CO gas abundance with radius in gas-rich protoplanetary disks. *Astrophys. J.* **883**, 98 (2019).
22. Zhang, K., Bosman, A. D. & Bergin, E. A. Excess C/H in protoplanetary disk gas from icy pebble drift across the CO snowline. *Astrophys. J. Lett.* **891**, L16 (2020).
23. Miotello, A. et al. Bright C_2H emission in protoplanetary discs in Lupus: high volatile C/O>1 ratios. *Astron. Astrophys.* **631**, A69 (2019).
24. Bergner, J. B. et al. A survey of C_2H, HCN, and $C^{18}O$ in protoplanetary disks. *Astrophys. J.* **876**, 25 (2019).
25. Semenov, D. et al. Chemistry in disks. *Astron. Astrophys.* **617**, A28 (2018).
26. Booth, A. S., van der Marel, N., Leemker, M., van Dishoeck, E. F. & Ohashi, S. A major asymmetric ice trap in a planet-forming disk. *Astron. Astrophys.* **651**, L6 (2021).
27. Dutrey, A. et al. Chemistry in disks. V. Sulfur-bearing molecules in the protoplanetary disks surrounding LkCa15, MWC480, DM Tauri, and GO Tauri. *Astron. Astrophys.* **535**, A104 (2011).

28. Le Gal, R. et al. Molecules with ALMA at planet-forming scales (MAPS). XII. Inferring the C/O and S/H ratios in protoplanetary disks with sulfur molecules. *Astrophys. J. Suppl. Ser.* **257**, 12 (2021).
29. Booth, A. S. et al. Sulphur monoxide emission tracing an embedded planet in the HD 100546 protoplanetary disk. *Astron. Astrophys.* **669**, A53 (2023).
30. Arun, R. et al. On the mass accretion rate and infrared excess in Herbig Ae/Be stars. *Astron. J.* **157**, 159 (2019).
31. Walsh, C. et al. ALMA hints at the presence of two companions in the disk around HD 100546. *Astrophys. J.* **791**, L6 (2014).
32. Fedele, D., Toci, C., Maud, L. T. & Lodato, G. ALMA 870 μm continuum observations of HD 100546. *Astron. Astrophys.* **651**, A90 (2021).
33. Quanz, S. P. et al. Confirmation and characterization of the protoplanet HD 100546 b—direct evidence for gas giant planet formation at 50 au. *Astrophys. J.* **807**, 64 (2015).
34. Currie, T. et al. Resolving the HD 100546 protoplanetary system with the gemini planet imager: evidence for multiple forming, accreting planets. *Astrophys. J.* **814**, L27 (2015).
35. Pinilla, P., Birnstiel, T. & Walsh, C. Sequential planet formation in the HD 100546 protoplanetary disk? *Astron. Astrophys.* **580**, A105 (2015).
36. Walsh, C., Daley, C., Facchini, S. & Juhász, A. CO emission tracing a warp or radial flow within 100 au in the HD 100546 protoplanetary disk. *Astron. Astrophys.* **607**, A114 (2017).
37. Bruderer, S., van Dishoeck, E. F., Doty, S. D. & Herczeg, G. J. The warm gas atmosphere of the HD 100546 disk seen by Herschel. Evidence of a gas-rich, carbon-poor atmosphere? *Astron. Astrophys.* **541**, A91 (2012).
38. Bruderer, S. Survival of molecular gas in cavities of transition disks. I. CO. *Astron. Astrophys.* **559**, A46 (2013).
39. Kama, M. et al. Volatile-carbon locking and release in protoplanetary disks. A study of TW Hya and HD 100546. *Astron. Astrophys.* **592**, A83 (2016).
40. Pineda, J. E. et al. High-resolution ALMA observations of HD 100546: asymmetric circumstellar ring and circumplanetary disk upper limits. *Astrophys. J.* **871**, 48 (2019).
41. Wichittanakom, C. et al. The accretion rates and mechanisms of Herbig Ae/Be stars. *Mon. Not. R. Astron. Soc.* **493**, 234–249 (2020).
42. Pirovano, L. M. et al. H_2O distribution in the disc of HD 100546 and HD 163296: the role of dust dynamics and planet–disc interaction. *Astron. Astrophys.* **665**, A45 (2022).
43. van Dishoeck, E. F. et al. Water in star-forming regions: physics and chemistry from clouds to disks as probed by Herschel spectroscopy. *Astron. Astrophys.* **648**, A24 (2021).
44. Francis, L. & van der Marel, N. Dust-depleted inner disks in a large sample of transition disks through long-baseline ALMA observations. *Astrophys. J.* **892**, 111 (2020).
45. Lovelace, R. V. E., Li, H., Colgate, S. A. & Nelson, A. F. Rossby wave instability of Keplerian accretion disks. *Astrophys. J.* **513**, 805–810 (1999).
46. Law, C. J. et al. Molecules with ALMA at planet-forming scales (MAPS). III. Characteristics of radial chemical substructures. *Astrophys. J. Suppl. Ser.* **257**, 3 (2021).
47. Zhang, K. et al. Molecules with ALMA at planet-forming scales (MAPS). V. CO gas distributions. *Astrophys. J. Suppl. Ser.* **257**, 5 (2021).
48. Guzmán, V. V. et al. Molecules with ALMA at planet-forming scales (MAPS). VI. Distribution of the small organics HCN, C_2H, and H_2CO. *Astrophys. J. Suppl. Ser.* **257**, 6 (2021).
49. Alarcón, F. et al. Molecules with ALMA at planet-forming scales (MAPS). VIII. CO gap in AS 209—gas depletion or chemical processing? *Astrophys. J. Suppl. Ser.* **257**, 8 (2021).
50. Ilee, J. D. et al. Molecules with ALMA at planet-forming scales (MAPS). IX. Distribution and properties of the large organic molecules HC_3N, CH_3CN, and c-C_3H_2. *Astrophys. J. Suppl. Ser.* **257**, 9 (2021).
51. van der Marel, N., Booth, A. S., Leemker, M., van Dishoeck, E. F. & Ohashi, S. A major asymmetric ice trap in a planet-forming disk. I. Formaldehyde and methanol. *Astron. Astrophys.* **651**, L5 (2021).
52. Panic, O. et al. Observations of warm molecular gas and kinematics in the disc around HD 100546. *Astron. Astrophys.* **519**, A110 (2010).
53. Miley, J. M. et al. Asymmetric mid-plane gas in ALMA images of HD 100546. *Mon. Not. R. Astron. Soc.* **485**, 739–752 (2019).
54. Fedele, D., Bruderer, S., van den Ancker, M. E. & Pascucci, I. On the asymmetry of the OH ro-vibrational lines in HD 100546. *Astrophys. J.* **800**, 23 (2015).
55. Nealon, R., Pinte, C., Alexander, R., Mentiplay, D. & Dipierro, G. Scattered light shadows in warped protoplanetary discs. *Mon. Not. R. Astron. Soc.* **484**, 4951–4962 (2019).
56. Young, A. K. et al. Chemical signatures of a warped protoplanetary disc. *Mon. Not. R. Astron. Soc.* **505**, 4821–4837 (2021).
57. Garufi, A. et al. The SPHERE view of the planet-forming disk around HD 100546. *Astron. Astrophys.* **588**, A8 (2016).
58. Follette, K. B. et al. Complex spiral structure in the HD 100546 transitional disk as revealed by GPI and MagAO. *Astron. J.* **153**, 264 (2017).
59. Lazareff, B. et al. Structure of Herbig AeBe disks at the milliarcsecond scale. *Astron. Astrophys.* **599**, A85 (2017).
60. Bohn, A. J. et al. Probing inner and outer disk misalignments in transition disks. Constraints from VLTI/GRAVITY and ALMA observations. *Astron. Astrophys.* **658**, A183 (2022).
61. Brittain, S. D., Najita, J. R. & Carr, J. S. High-resolution near-infrared spectroscopy of HD 100546. IV. Orbiting companion disappears on schedule. *Astrophys. J.* **883**, 37 (2019).
62. Sissa, E. et al. High-contrast study of the candidate planets and protoplanetary disk around HD 100546. *Astron. Astrophys.* **619**, A160 (2018).
63. Pérez, S. et al. Long baseline observations of the HD 100546 protoplanetary disk with ALMA. *Astrophys. J.* **889**, L24 (2020).
64. Zhu, Z., Stone, J. M., Rafikov, R. R. & Bai, X. Particle concentration at the planet induced gap edges and vortices I. Iinviscid three dimensional hydro disks. *Astrophys. J.* **785**, 122 (2014).
65. Norfolk, B. et al. The origin of the Doppler-flip in HD 100546: a large scale spiral arm generated by an inner binary companion. *Astrophys. J. Lett.* **936**, L4 (2022).
66. Wright, C. M. et al. Resolving structure of the disc around HD100546 at 7 mm with ATCA. *Mon. Not. R. Astron. Soc.* **453**, 414–438 (2015).
67. Mendigutía, I. et al. The protoplanetary system HD 100546 in Hα polarized light from SPHERE/ZIMPOL. A bar-like structure across the disk gap? *Astron. Astrophys.* **608**, A104 (2017).
68. Debes, J. H. et al. Chasing shadows: rotation of the azimuthal asymmetry in the TW Hya disk. *Astrophys. J.* **835**, 205 (2017).
69. Loomis, R. A. et al. Detecting weak spectral lines in interferometric data through matched filtering. *Astron. J.* **155**, 182 (2018).
70. Carney, M. T. et al. Increased H_2CO production in the outer disk around HD 163296. *Astron. Astrophys.* **605**, A21 (2017).
71. Booth, A. S. et al. Sulphur monoxide exposes a potential molecular disk wind from the planet-hosting disk around HD 100546. *Astron. Astrophys.* **611**, A16 (2018).
72. Gaia Collaboration Gaia Data Release 2. Summary of the contents and survey properties. *Astron. Astrophys.* **616**, A1 (2018).
73. Pickles, A. J. A stellar spectral flux library: 1150–25000 Å. *Publ. Astron. Soc. Aust.* **110**, 863–878 (1998).

74. Woodall, J., Agúndez, M., Markwick-Kemper, A. J. & Millar, T. J. The UMIST database for astrochemistry 2006. *Astron. Astrophys.* **466**, 1197–1204 (2007).
75. Cleeves, L. I., Bergin, E. A. & Harries, T. J. Indirect detection of forming protoplanets via chemical asymmetries in disks. *Astrophys. J.* **807**, 2 (2015).

Acknowledgements

We acknowledge D. Fedele for sharing the ALMA 870 μm continuum data. L.K. acknowledges funding via a Science and Technology Facilities Council (STFC) studentship. E.F.v.D. is supported by A-ERC grant agreement no. 101019751 MOLDISK. M.N.D. acknowledges the Swiss National Science Foundation (SNSF) Ambizione grant no. 180079, the Center for Space and Habitability (CSH) Fellowship, and the IAU Gruber Foundation Fellowship. C.W. acknowledges financial support from the University of Leeds, the Science and Technology Facilities Council, and UK Research and Innovation (grant numbers ST/T000287/1 and MR/T040726/1).

Author contributions

L.K. reduced the ACA CS data, ran the chemical models, performed analysis of both the data and models, and wrote the manuscript. M.K. contributed to the analysis of both the data and models, original research concepts and writing of the manuscript, and led the proposal for the ACA data. A.S.B. provided the ALMA SO data and contributed to the writing of the manuscript. E.A.B., L.I.C., E.F.v.D., M.N.D., K.F., J.R., O.S. and C.W. contributed to the writing of the manuscript.

Competing interests

The authors declare no competing interests.

Additional information

Extended data is available for this paper at https://doi.org/10.1038/s41550-023-01951-9.

Supplementary information The online version contains supplementary material available at https://doi.org/10.1038/s41550-023-01951-9.

Correspondence and requests for materials should be addressed to Luke Keyte.

Peer review information *Nature Astronomy* thanks Zhaohuan Zhu, Rebecca Nealon and Alison Young for their contribution to the peer review of this work.

https://doi.org/10.1038/s41550-023-01951-9

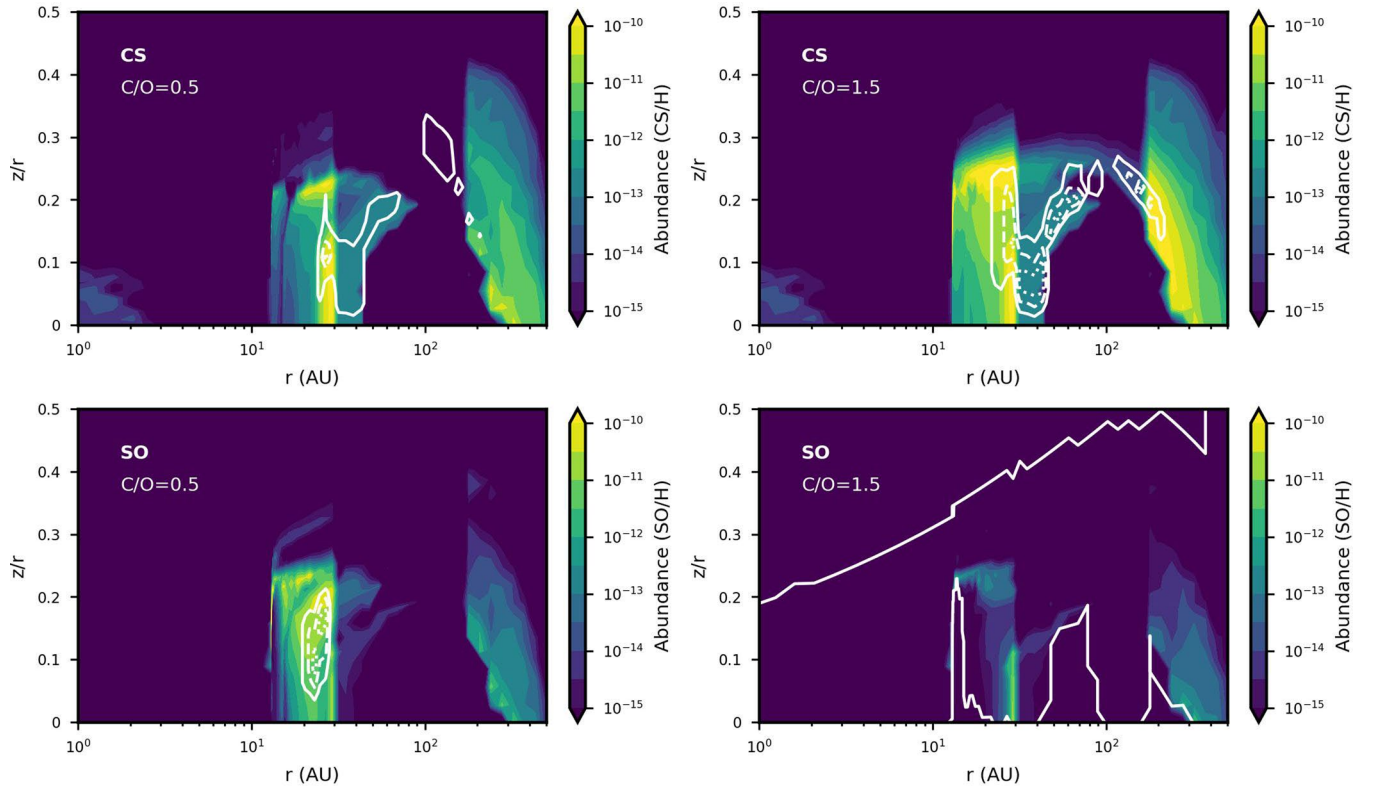

Extended Data Fig. 1 | Abundance maps and contribution functions for the modelled CS and SO emission in HD 100546. Each panel shows an abundance map overlaid with contours representing 25% and 75% line emission (white). Top row: CS 7-6 emission from the C/O=0.5 region (left) and C/O>1 region (right). Bottom row: SO $7_7 - 6_6 + 7_8 - 6_7$ emission from the C/O=0.5 region (left) and C/O>1 region (right).

https://doi.org/10.1038/s41550-023-01951-9

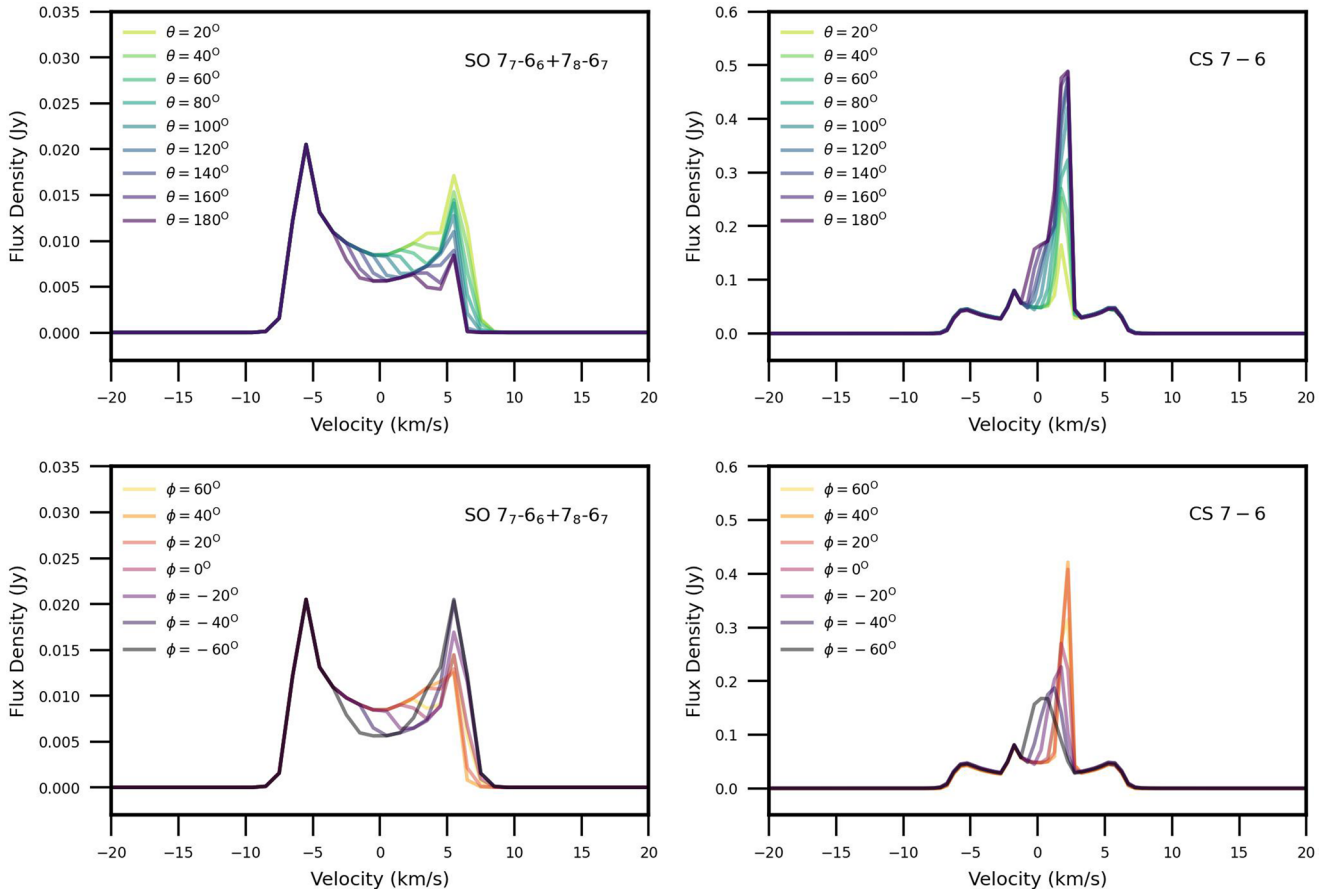

Extended Data Fig. 2 | Effect of varying the high-C/O wedge size and position on the modelled spectra. Top row: SO $7_7 - 6_6 + 7_8 - 6_7$ (left) and CS 7-6 (right) spectra for variations in wedge size (θ), centered on position $\phi = 0$. Bottom panel: SO $7_7 - 6_6 + 7_8 - 6_7$ (left and CS 7-6 (right) spectra for variations in wedge position (ϕ), for a fixed angular size $\theta = 60°$.

https://doi.org/10.1038/s41550-023-01951-9

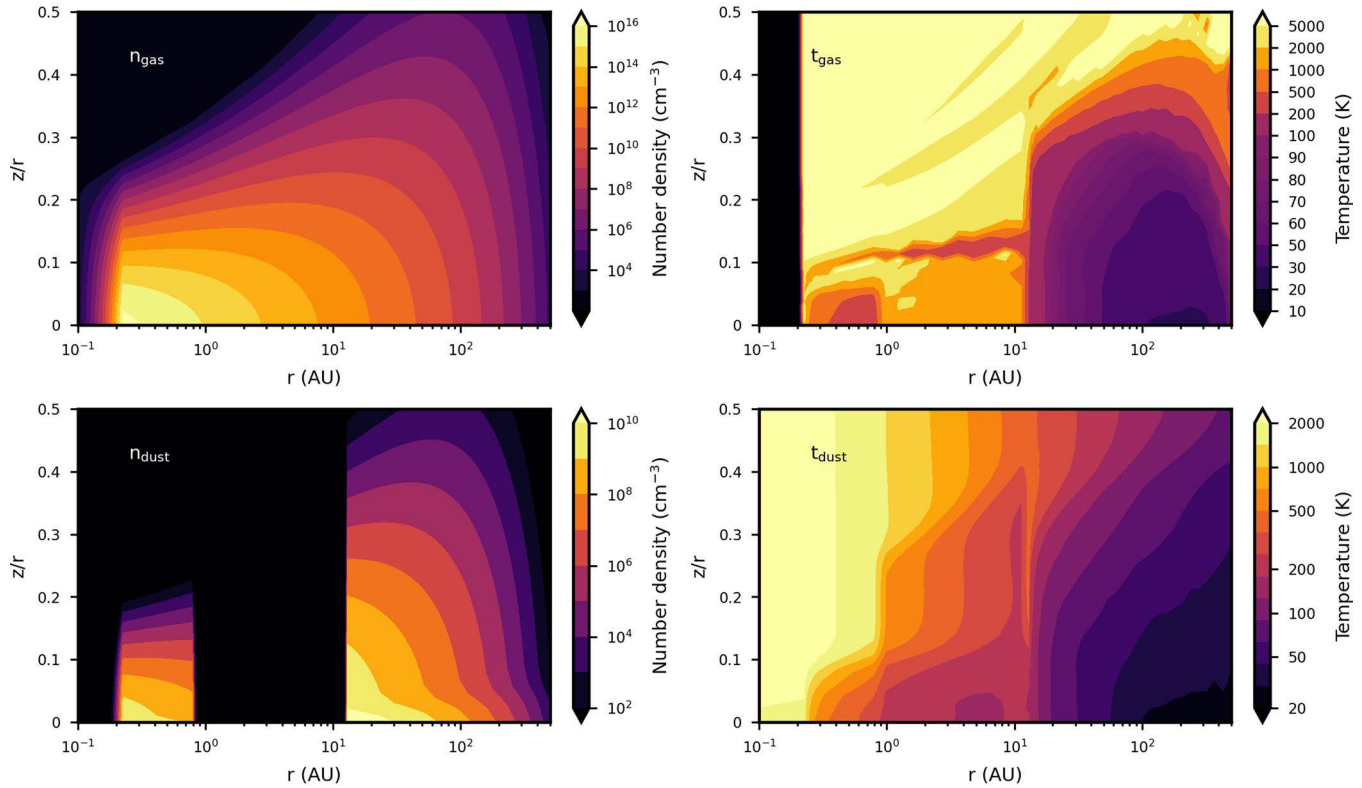

Extended Data Fig. 3 | Temperature and density maps for the baseline HD 100546 disk model (C/O=0.5). Top left: Gas number density. Bottom left: Dust number density. Top right: Gas temperature. Bottom right: Dust temperature.